The Astrophysical Journal, 900:57 (14pp), 2020 September 1 https://doi.org/10.3847/1538-4357/abad2f

Implications of Symmetry and Pressure in Friedmann Cosmology. III. Point Sources of Dark Energy that Tend toward Uniformity

K. S. Croker[1], J. Runburg[1], and D. Farrah[1,2]
[1] Department of Physics and Astronomy, University of Hawai'i at Mānoa, 2505 Correa Road, Honolulu, HI 96822, USA; kcroker@phys.hawaii.edu
[2] Institute for Astronomy, University of Hawai'i, 2680 Woodlawn Drive, Honolulu, HI 96822, USA
Received 2019 February 12; revised 2020 July 11; accepted 2020 July 24; published 2020 September 1

Abstract

We show that point sources of dark energy can explain accelerated late-time expansion and, simultaneously, satisfy observational constraints on massive compact objects. Population III stellar collapse into GEneric Objects of Dark Energy (GEODEs) between $8 \lesssim z \lesssim 20$ mimics the observed Ω_Λ within the typical concordance cosmology. We determine the appropriate dynamical model of aggregate GEODE flow within covariant linear perturbation theory. We find that all continuum fluid properties, at large scales, are determined by the internal properties and spin of individual GEODEs. For large spin, the spatial distribution of GEODEs becomes uniform on scales $\lesssim$200 Mpc. The power spectrum of cold dark matter is essentially unaltered. A Population III GEODE scenario provides an observationally consistent physical origin for accelerated late-time expansion while imposing no new constraints on structure formation.

Unified Astronomy Thesaurus concepts: Cosmological perturbation theory (341); Dark energy (351); Population III stars (1285); Relativistic cosmology (1387)

1. Introduction

The accelerated expansion of the universe, established by Riess et al. (1998) and Perlmutter et al. (1999), provided the first evidence of what has come to be called dark energy (DE). Within the Friedmann–Robertson–Walker (FRW) cosmological framework, DE is readily modeled as a constant density ρ_Λ, uniform in space and constant in time. All present data (e.g., Aghanim et al. 2018) are consistent with this simplest explanation and produce a value of $\rho_\Lambda \sim 0.7\rho_{cr}$ today.

This number, the cosmological constant, is widely regarded as problematic. From the perspective of quantum field theories, ρ_Λ should either be exactly zero or related to some fundamental energy scale. As it so happens, ρ_Λ is related to another known quantity: $\rho_\Lambda \sim 2\rho_m$, the average matter density in the universe, today. This suggests that the "cosmological constant" may not actually be constant, but is instead dynamically related to the matter content of the universe.

Numerous investigations over the past 20 years (see Amendola & Tsujikawa 2010 and references therein) have pursued this theme. One prominent strategy is the introduction of additional dynamical fields. Another prominent strategy is to include effective source terms from small-scale inhomogeneities. With respect to the latter, arguments are put forth that the FRW framework is not entirely appropriate for the study of our universe. It is asserted that "backreaction," due to nonlinearities in Einstein's equations, conspires to produce an effective ρ_Λ that acts in Friedmann's equation.

Recently, Croker & Weiner (2019, Section 2) established that FRW models can be reliably used and are backreaction-free, given the following caveats:

1. Einstein's equations are determined via the Hilbert action
2. the Robertson–Walker (RW) metric is the lowest-order term in a convergent perturbation series
3. in the absence of an explicit nongravitational Lagrange density, constraints on nongravitational fields are forbidden before equations of motion are produced.

The consequence of these caveats is that pressures interior to compact objects must be spatially averaged to compute the Friedmann (i.e., zero-order) source terms. For stars, planets, and gas, internal pressures are negligible relative to their mass energy densities. In this limit, dynamics consistent with the naive application of Birkhoff's theorem are obtained. For objects composed of ultrarelativistic material, Birkhoff's theorem cannot be applied on cosmological timescales, because such material can become cosmologically coupled.

This result takes on particular significance, given any population of GEneric Objects of Dark Energy (GEODEs). GEODEs are stellar collapse remnants, first proposed by Gliner (1966), composed mostly of DE. Croker & Weiner (2019, Section 4.2) show that the mass of each individual GEODE can cosmologically blueshift:

$$m \propto a^3, \tag{1}$$

where a is the RW scale factor. This energy shift is analogous to the familiar photon redshift. Because GEODEs, in bulk, comove with the Hubble flow, their cosmological number density diminishes:

$$n \propto 1/a^3. \tag{2}$$

The cosmological GEODE energy density, mn, then becomes constant in space and time. For example, if a reasonable fraction of Population III stars collapse to GEODEs before reionization, the measured ρ_Λ is flexibly obtained. In other words, pointlike sources of DE provide a previously overlooked third strategy to explain the value of ρ_Λ.

1.1. The MACHO Problem

Given that GEODEs are compact objects formed from matter, it is natural to expect that their bulk dynamics would track those of cold dark matter (CDM). Specifically, one would

expect GEODEs to "clump" with CDM and eventually become a subpopulation of MAssive Compact Halo Objects (MACHOs). If formed at $z \sim 15$, Population III GEODEs would blueshift into 10^3–10^5 $M_\odot$ GEODEs today and would mimic intermediate-mass black holes (IMBHs), on which there are observational constraints.

The IMBH mass range has been previously investigated as candidate objects for CDM halos. For compact objects in the IMBH mass range, the most powerful constraint comes from the existence of binary star systems within the Milky Way. Binney & Tremaine (2008, (8.65b)) give the timescale for catastrophic disruption of binary star systems as

$$t_{d,\mathrm{cat}} \simeq \frac{0.07}{\rho_{\mathrm{dis}}}\sqrt{\frac{M_{\mathrm{b}}}{GA^3}}, \tag{3}$$

where ρ_{dis} is the mass density of disruptors, M_{b} is the mass of the binary system, and A is the semimajor axis[3] of the binary orbit. Systems are considered vulnerable to disruption if this timescale is less than the lifetime of the Milky Way, roughly 10 Gyr. Due to the scaling $1/A^{3/2}$, wide binaries are more easily disrupted.

To develop constraints on MACHOs, one studies halo wide binaries: those binary pairs that have a center-of-mass orbit that takes the system far from the galactic plane. Monroy-Rodríguez & Allen (2014, Table 3) report observations of several such stellar pairs. Adopting the pair with the largest semimajor axis and requiring $t_{d,\mathrm{cat}}$ to exceed the age of the universe, we find

$$\rho_{\mathrm{dis}} \lesssim 8 \times 10^{-24}\ \mathrm{kg\ m^{-3}}. \tag{4}$$

While this is 10^3 larger than ρ_{cr}, if Population III GEODEs behave as CDM, it is natural to expect that their local densities far exceed background values. It becomes clear that any viable pointlike DE explanation of ρ_Λ must dynamically keep Population III GEODE densities low in regions of CDM.

In this paper, we address the MACHO problem by studying the dynamical behavior of Population III GEODEs. The structure of this paper is as follows. In Section 2, we provide definitions necessary to pose Einstein's equations perturbatively. In Section 3, we review the zero-order (i.e., Friedmann) cosmological source appropriate for a GEODE species. In Section 4, we determine the first-order stress perturbations appropriate for a GEODE species. In Section 5, we determine the dynamical equations that govern the evolution of these stress perturbations. In Section 6, we present results from numerical solutions of these dynamical equations. In Section 7, we interpret these results physically and discuss relations between Kerr BHs and GEODEs. In Section 8, we briefly conclude.

1.2. Conventions and Units

Throughout this work, unless otherwise indicated, we use the following units: densities are in the critical density today ρ_{cr}, times are in the reciprocal Hubble rate today H_0^{-1}, and Fourier wavenumber k is in Mpc^{-1}. We make every attempt to use the same notation as Hu (2004). We adopt cosmological parameters from the TT,TE,EE+lowE+lensing+BAO Planck 2018 cosmology, given by Aghanim et al. (2018, Table 2). For consistency with structure formation literature, all densities will be physical (as opposed to comoving). We will often refer to redshifts and scale factors as "times." No confusion will arise because these quantities evolve monotonically in any realistic Friedmann model.

[3] Because we use a for the scale factor extensively, we have changed to A for binary semimajor axis.

2. Definitions and Assumptions

In this section, we review sufficient definitions and assumptions to establish a well-defined cosmological perturbation theory from Einstein's equations. This will be a brief review of Croker & Weiner (2019, Section 2) and then an explicit definition of the coordinates and frame fields required for correct application of this formalism at first order. The fundamental assumption is that Einstein's equations are valid. This means that a unique and bounded (i.e., well-defined) metric and stress tensor exist everywhere and for all time. The goal is to efficiently reconstruct them from observation.

2.1. RW Coordinates and RW Frame Fields

We adopt the following spatially flat RW metric representation:

$$g_{\mu\nu}(\eta, \boldsymbol{x}) \coloneqq a(\eta)^2[\eta_{\mu\nu} + \epsilon\, h^{(1)}_{\mu\nu}(\eta, \boldsymbol{x}) + \cdots] \qquad \epsilon < 1. \tag{5}$$

This is the definition given by Croker & Weiner (2019, Equation (14)), abbreviated[4] at first order. Croker & Weiner (2019, Sections 3.2–3.4) show that the coordinates η and $\boldsymbol{x}$ continue to make sense inside many ultrarelativistic compact objects. We will assume that they are well defined everywhere, and we will use only these coordinates. The metric representation in Equation (5) is given with respect to a class of coordinate frame fields spanned by nonnormal, and possibly nonorthogonal, bases $\{\partial_\mu\}$. We will call these frame fields "RW frame fields."

RW frame fields are useful because they are spanned by coordinate bases. The explicit prescription of coordinate functions then allows explicit computation of representations. Across the differentiable manifold $\mathcal{M}$, RW frames differ at most by order ϵ quantities. Taken together, RW frames can be constructed to give representations that closely approximate nonrelativistic mechanics on large regions of spacetime. Note that first-order equations of motion are produced from variation of the $h^{(1)}_{\mu\nu}$. This means that source terms to Einstein's equations for the metric perturbation degrees of freedom must be tensor components in some RW frame field.

2.2. The Eigenframe Fields

The stress tensor $T_{\mu\nu}$ is, by definition, proportional to the variation of the nongravitational Lagrange density with respect to the true (i.e., unapproximated) inverse metric. Unfortunately, we do not know the true metric, only that it uniquely exists. We may, however, leverage this uniqueness to give an invariant description of the true stress tensor.

[4] For clarity, we write only the first-order perturbations, have removed details of the domain of definition, and removed details of convergence and differentiability properties of the full series. These are not relevant for our present discussion, but are given in op. cit. precisely.

The tensor $T_{\mu\nu}$ can be regarded as a linear map from each tangent space at a point P to its dual space at P,

$$T_{\mu\nu}\colon T_P\mathcal{M} \to T_P^*\mathcal{M}. \tag{6}$$

In other words, "$T_{\mu\nu}$ acting on an index up quantity produces an index down quantity." If we contract with the inverse metric at P, we produce a linear operator T on $T_P\mathcal{M}$,

$$T \coloneqq g^{\mu\alpha}T_{\alpha\nu}\colon T_P\mathcal{M} \to T_P\mathcal{M}. \tag{7}$$

The operator T decomposes into the sum of a diagonalizable operator T_{I} and a nilpotent[5] operator T_{II}. The diagonalizable operator T_{I} describes timelike stress, while the nilpotent operator T_{II} describes lightlike stress.

At any point P, T_{I} has one timelike and three spacelike eigenvectors. If the type I stress at P has no particular symmetries, as expected in general, these eigenvectors define a unique frame field $\{\bar{e}_\mu\}$ (up to permutations in order and sign). If there are symmetries at P, then there are repeat eigenvalues and many such frames at P. We will call these frame fields "eigenframe fields." We will distinguish quantities in an eigenframe field with an overline.

Eigenframe fields are useful because they give an invariant characterization of the stress tensor. In any eigenframe field, the representation of T_{I} is diagonal:

$$\overline{T^{\mathrm{I}}_{\mu\nu}} = \mathrm{diag}[\overline{\rho}, \overline{p[1]}, \overline{p[2]}, \overline{p[3]}], \tag{8}$$

where the energy density $\overline{\rho}$ and principal pressures $\overline{p[\ell]}$ are the eigenvalues of T_{I} at P. In other words, the components of the stress tensor in an eigenframe are invariant, physical quantities. Suppose the timelike eigenvalue is unique. Then the timelike eigenvector $\bar{e}_0$ becomes the velocity of the type I stress at P, if viewed from any noneigenframe at P. From the perspective of eigenframe fields, material that can be at rest is at rest.

3. Population III GEODE Stress at Zero Order

In this section, we will establish the appropriate dynamics of a GEODE source within Friedmann cosmology. Friedmann's acceleration equation is sourced by the flat space average of the stress tensor's trace:

$$\frac{d^2a}{d\eta^2} = -\frac{4\pi G}{3}a^3\langle T^\mu_\mu(\eta, \boldsymbol{x})\rangle_{\mathcal{V}}. \tag{9}$$

The average may be taken over any volume larger than the homogeneity scale $\mathcal{V}^{1/3}$. The trace is an invariant scalar, so we express its value in any eigenframe field,

$$\frac{d^2a}{d\eta^2} = \frac{4\pi G}{3}a^3\left\langle \overline{\rho}(\eta, \boldsymbol{x}) - \sum_{\ell=1}^{3}\overline{p[\ell]}(\eta, \boldsymbol{x})\right\rangle_{\mathcal{V}}. \tag{10}$$

Note the distinction between the coordinates (RW coordinates) and components in a frame (an eigenframe). Define

$$\rho \coloneqq \langle\overline{\rho}(\eta, \boldsymbol{x})\rangle_{\mathcal{V}}, \tag{11}$$

$$p \coloneqq \frac{1}{3}\left\langle\sum_{\ell=1}^{3}\overline{p[\ell]}(\eta, \boldsymbol{x})\right\rangle_{\mathcal{V}}. \tag{12}$$

[5] I.e., $T^2_{\mathrm{II}} = 0$.

Because averages are linear, we may decompose the energy density and pressure into a sum over constituents:

$$\rho = \sum_J \rho_J \tag{13}$$

$$p = \sum_J p_J. \tag{14}$$

Now presume an ensemble of Population III GEODEs. Denote GEODE constituent quantities with a subscript G. We will consider a single, but arbitrary, GEODE species. The equation of state for the GEODE contribution is the ratio

$$w_G \coloneqq \frac{p_G}{\rho_G}; \tag{15}$$

any causal deviation from perfect de Sitter spheres will lead to an equation of state greater than -1. We define

$$p_G \coloneqq (-1 + \chi)\rho_G, \tag{16}$$

with the constant $\chi \geqslant 0$ characterizing this deviation. Consider a burst formation of GEODEs from baryons at time a_G, sufficient to produce Ω_Λ at the present day. Then, conservation of stress energy requires that

$$\rho_G(a) = \begin{cases} 0 & a < a_G \\ \Omega_\Lambda a^{-3\chi} & a \geqslant a_G. \end{cases} \tag{17}$$

Let ρ_b denote the baryon density and let Ξ denote the fraction of baryons consumed to produce GEODEs at a_G. In order to recover the correct Ω_Λ measured today,

$$\Xi \coloneqq \frac{\Omega_\Lambda}{\Omega_b}a_G^{3(1-\chi)}. \tag{18}$$

4. Population III GEODE Stress at First Order

In the previous section, we determined the perturbative zero-order solution. This solution is a necessary input for the first-order equations that describe position-dependent degrees of freedom. In this section, we will characterize the nongravitational source terms appropriate for the first-order equations. It will be important to distinguish between unapproximated quantities and Fourier transforms or averages that use the same symbol. We will denote unapproximated quantities with a superscript $\boldsymbol{x}$ notation.

The action principle unambiguously determines Einstein's equations at first order. In Newtonian gauge, the following matter sources appear:

$$\begin{aligned}\delta\rho^{\boldsymbol{x}} &= \rho^{\boldsymbol{x}} - \rho \\ \delta p^{\boldsymbol{x}}[\ell] &= p^{\boldsymbol{x}}[\ell] - \langle p^{\boldsymbol{x}}[\ell]\rangle_{\mathcal{V}}.\end{aligned} \tag{19}$$

Gauge, in this context, means coordinates whose partials define RW frame fields. In the Newtonian gauge, coordinates are constructed to set $h^{(1)}_{\mu\nu} = 0$ for $\mu \neq \nu$. The metric perturbations are defined in an RW frame field, so these sources are components of the stress tensor in the same RW frame field.

Regarded as a 3×3 spatial strain tensor, the principal pressures are typically decomposed under Euclidean rotations. The trace,

$$\delta p^{\boldsymbol{x}} \coloneqq \frac{1}{3}\sum_{\ell=1}^{3}\delta p^{\boldsymbol{x}}[\ell], \tag{20}$$

is called the "isotropic pressure perturbation." The residual,

$$p(\Pi^j_k)^{\boldsymbol{x}} := \begin{cases} \frac{2}{3}\delta p^{\boldsymbol{x}}[j] - \frac{1}{3}\sum_{\ell\neq j}\delta p^{\boldsymbol{x}}[\ell] & j = k \\ 0 & j \neq k, \end{cases} \tag{21}$$

is called the "anisotropic stress."

4.1. Definition of the Continuum Fluid Approximation

Astrophysical sources will contribute energy densities and principal pressures that greatly exceed the background averages. More so, these large deviations from the background only occur at the positions of the sources. Typically then, $\delta\rho^{\boldsymbol{x}}$, $\delta p^{\boldsymbol{x}}$, and $(\Pi^j_k)^{\boldsymbol{x}}$ are regarded as continuum fluid approximations. In the continuum fluid approximation (e.g., Landau & Lifshitz 1959, Section 1), one coarse-grains the source into "fluid elements." The fluid elements must be large enough so that a bulk description is useful on the desired scales. The fluid elements must also be small enough so that four-momentum is distributed within the elements faster than between them. An average is then performed over each fluid element volume to produce density and pressure fields.

Unfortunately, no quantitative prescription is given for any part of this procedure. In other words, the ambiguity resolved by Croker & Weiner (2019) at zero order reemerges in the first-order theory. A spatial average must be taken, but no length scale over which to average, or Jacobian to use during integration, is unambiguously prescribed.

In Fourier space, however, this pathology is bypassed. In practice, the Fourier expansion is always truncated at some finite $k_{\max}$. Upon inversion of the transform, this leads to first-order real-space sources that are low-pass filtered below $2\pi/k_{\max}$. All of the resulting dynamical variables now smoothly track the distribution in real space of the pointlike objects. In fact, there is a measured scale $2\pi/k_{\rm nl}$ (Dodelson 2003, Section 7.1.1), above which the observed matter power spectrum agrees with linear theory predictions. This scale defines a continuum fluid approximation. It is the first-order analog to the zero-order homogeneity scale $\mathcal{V}^{1/3}$. In summary,

1. a well-defined, first-order theory requires the Fourier transforms of Equations (19), not the Fourier transforms of the continuum fluid approximations to Equations (19).

In particular, pressures interior to all objects will get "smeared" into all modes below $k_{\max}$. For ensembles of ultrarelativistic objects, peculiar flows at first order can then become influenced by these objects' internal dynamics. This is the same phenomenon observed at zero order, but replayed at first order.

4.2. Existence of Fourier Transforms

We have used Fourier transforms to produce a well-defined continuum fluid approximation from the actual first-order sources to Einstein's equations. D'Eath (1976, Section 3) proves that solutions to Einstein's equations for perturbed RW spaces with spatial curvature $\Omega_K := 0$ do not generally exist unless perturbations decay sufficiently fast at infinity. This pathology implies that the Fourier transforms of Equation (19) may diverge.

The standard approach (e.g., Peebles 1980, Section 27) regards the universe as "box periodic." This procedure changes the global topology of the universe to that of a three-torus. We adopt this convention and define spatial Fourier transforms on a three-torus with radii much larger than the zero-order homogeneity scale $\mathcal{V}^{1/3}$.

4.3. Ensemble Definition, Interpretation of Zero-order χ

In this section, we define the GEODE ensemble in terms of a local model and use it to compute the background equation of state $-1+\chi$. In order that our definition be invariant, we must work in an eigenframe field. Regard $\overline{\rho^{\boldsymbol{x}}_G}$ and $\overline{p^{\boldsymbol{x}}_G}$ as being sourced by a population of N GEODEs at positions $\boldsymbol{x}_j(\eta)$:

$$\begin{aligned} \overline{\rho^{\boldsymbol{x}}_G} &:= \sum_j^N [u(\eta) + \overline{\kappa_0}(\eta, \boldsymbol{x} - \boldsymbol{x}_j)]\mathbf{1}_{\mathcal{B}_j} \\ \overline{p^{\boldsymbol{x}}_G} &:= \sum_j^N [-u(\eta) + \overline{\kappa_1}(\eta, \boldsymbol{x} - \boldsymbol{x}_j)]\mathbf{1}_{\mathcal{B}_j}. \end{aligned} \tag{22}$$

Each GEODE is defined on a support of radius[6] R centered at $\boldsymbol{x}_j(\eta)$,

$$\mathbf{1}_{\mathcal{B}_j}(\boldsymbol{x}) := \begin{cases} 1 & |\boldsymbol{x} - \boldsymbol{x}_j(\eta)| \leqslant R \\ 0 & |\boldsymbol{x} - \boldsymbol{x}_j(\eta)| > R, \end{cases} \tag{23}$$

and separated into a de Sitter portion with uniform energy density u and a superposed "crust." The crust is characterized by an energy density $\overline{\kappa_0}$ and an isotropic pressure $\overline{\kappa_1}$.

From Equation (16), it follows that

$$\frac{1}{\mathcal{V}}\sum_j^N \int_{\mathcal{B}_j} [(-1+\chi)(u + \overline{\kappa_0}) + u - \overline{\kappa_1}]\, d^3x = 0. \tag{24}$$

All GEODEs are presumed identical, so

$$\frac{N\mathcal{B}}{\mathcal{V}}[(-1+\chi)(u + \langle\overline{\kappa_0}\rangle_{\mathcal{B}}) + u - \langle\overline{\kappa_1}\rangle_{\mathcal{B}}] = 0. \tag{25}$$

Rearranging, and assuming that $\langle\overline{\kappa_0}\rangle_{\mathcal{B}} \ll u$, the binomial expansion gives

$$\chi = \frac{\langle\overline{\kappa_1} + \overline{\kappa_0}\rangle_{\mathcal{B}}}{u} + \cdots. \tag{26}$$

At leading order, χ is the GEODE volume-averaged sum of the crust energy density and pressure, scaled by the GEODE interior DE density.

4.4. GEODE Perturbations, Interpretation of c_G^2

In Fourier space, Hu (2004, Equation (106)) defines the squared nonadiabatic sound speed c_G^2 as

$$c_G^2(\boldsymbol{k}, \eta) := \left.\frac{\delta p_G(\boldsymbol{k}, \eta)}{\delta\rho_G(\boldsymbol{k}, \eta)}\right|_{\rm GEODErest}. \tag{27}$$

For point objects, the "rest" gauge for a particular constituent comoves[7] with the peculiar flow of that constituent. GEODEs are extended objects, so the "rest" gauge perceives mass centers to be at rest. These RW frame fields are not, however, fully adapted to individual GEODEs. They will still perceive intrinsic GEODE motions, such as spin. For this reason, we do not use the word "rest." Instead, we will refer to this gauge as the GEODE "flow gauge."

[6] This magnitude is defined with respect to the Euclidean norm.

[7] In other words, the "energy flux" T^0_k contribution from this specific constituent vanishes. See comments below (Bardeen 1980, Equation (3.13)).

From Equations (19) and (22), the Fourier transforms δp_G and $\delta\rho_G$ will track the GEODE distribution in space at modes below $\sim 1/R$, due to the presence of many $\mathbf{1}_{\mathcal{B}_j}$. This remains true in the flow gauge, so c_G^2 is constant in space for modes below $\sim 1/R$. We use this to compute c_G^2 directly from the Fourier transforms. For $k \ll 2\pi/R$, we have that

$$\int e^{i\boldsymbol{k}\cdot\boldsymbol{x}}(p_G^{\boldsymbol{x}} - p_G)\, d^3x = c_G^2 \int e^{i\boldsymbol{k}\cdot\boldsymbol{x}}(\rho_G^{\boldsymbol{x}} - \rho_G)\, d^3x. \tag{28}$$

At $\boldsymbol{k} = 0$, the computation is just a spatial average and the fluctuations vanish, independently of c_G^2. Consider $\boldsymbol{k} \neq 0$. By orthogonality, all spatially independent contributions vanish:

$$\int e^{i\boldsymbol{k}\cdot\boldsymbol{x}} p_G^{\boldsymbol{x}}\, d^3x = c_G^2 \int e^{i\boldsymbol{k}\cdot\boldsymbol{x}} \rho_G^{\boldsymbol{x}}\, d^3x. \tag{29}$$

Substitution of Equations (22), formally transformed into the flow gauge, gives

$$\int e^{i\boldsymbol{k}\cdot\boldsymbol{x}} \sum_j^N [\kappa_1 - u - c_G^2(\kappa_0 + u)]\mathbf{1}_{\mathcal{B}_j}\, d^3x = 0. \tag{30}$$

The pure de Sitter contributions are invariant because pure DE is a multiple of the metric. We may use the supports of the individual GEODEs to reexpress the transform as a sum over the ensemble

$$\sum_j^N \int_{\mathcal{B}_j} e^{i\boldsymbol{k}\cdot\boldsymbol{x}} [\kappa_1 - u - c_G^2(\kappa_0 + u)]\, d^3x = 0. \tag{31}$$

From each term, factor out the constant phase $\exp(i\boldsymbol{k}\cdot\boldsymbol{x}_j)$:

$$\sum_j^N e^{i\boldsymbol{k}\cdot\boldsymbol{x}_j} \int_{\mathcal{B}_j} e^{i\boldsymbol{k}\cdot(\boldsymbol{x}-\boldsymbol{x}_j)} [\kappa_1 - u - c_G^2(\kappa_0 + u)]\, d^3x = 0. \tag{32}$$

On each support, $|\boldsymbol{k}| \ll 1/R$, so the exponential under the integral is essentially 1,

$$\sum_j^N e^{i\boldsymbol{k}\cdot\boldsymbol{x}_j} \int_{\mathcal{B}_j} \kappa_1 - u - c_G^2(\kappa_0 + u)\, d^3x = 0. \tag{33}$$

Performing the integrations gives

$$\mathcal{B}\sum_j^N e^{i\boldsymbol{k}\cdot\boldsymbol{x}_j} [\langle\kappa_1\rangle_{\mathcal{B}_j} - u - c_G^2(\langle\kappa_0\rangle_{\mathcal{B}_j} + u)] = 0. \tag{34}$$

Because all GEODEs are presumed identical, the term in square braces can be factored out:

$$[\langle\kappa_1\rangle_{\mathcal{B}} - u - c_G^2(\langle\kappa_0\rangle_{\mathcal{B}} + u)] \sum_j^N e^{i\boldsymbol{k}\cdot\boldsymbol{x}_j} = 0. \tag{35}$$

If the sum happens to vanish at the fixed $\boldsymbol{k}$ we have chosen, no constraint on c_G^2 can be established. In Appendix A, we prove that the sum of phases is nonzero almost everywhere in $\boldsymbol{k}$ for any distribution of N GEODEs in space. So if the sum vanishes, there always exists $\tau \in \mathbb{R}^3$ with $|\tau|$ arbitrarily small so that the sum does not vanish at $\boldsymbol{k} + \tau$. In this sense, we may always divide by the sum to arrive at the desired relation,

$$c_G^2 = \frac{-u + \langle\kappa_1\rangle_{\mathcal{B}}}{u + \langle\kappa_0\rangle_{\mathcal{B}}}. \tag{36}$$

In order to express this parameter in terms of intrinsic GEODE properties, we must express the flow gauge stress components in terms of eigenvalues. Pick any GEODE. The flow frames near this GEODE perceive only higher-order center-of-mass motion. Pick a flow frame at some point P in the GEODE crust. Suppose that this flow frame perceives the crust in motion, spinning at velocity $\beta(\eta, \boldsymbol{x})$ in some direction denoted $\hat{\phi}$. The transformation from an eigenframe at P to the flow frame at P is detailed in Appendix B. After transformation, the crust energy density becomes

$$\kappa_0 = \gamma^2(\overline{\kappa_0} + \beta^2\overline{\kappa_1}) + O(\epsilon), \tag{37}$$

while the crust principal pressures become

$$p_G^{\boldsymbol{x}}[\hat{\phi}] = \gamma^2(\overline{\kappa_1} + \beta^2\overline{\kappa_0}) + O(\epsilon) \tag{38}$$

$$p_G^{\boldsymbol{x}}[\hat{r}] = \overline{\kappa_1} + O(\epsilon) \tag{39}$$

$$p_G^{\boldsymbol{x}}[\hat{\theta}] = \overline{\kappa_1} + O(\epsilon). \tag{40}$$

The frames are related by a boost, with order ϵ corrections. Because c_G^2 relates two order-ϵ quantities, these corrections are to be dropped. By definition, κ_1 is the isotropic pressure in the flow gauge, so

$$\kappa_1 = \frac{1}{3}\left(2\overline{\kappa_1} + \frac{\overline{\kappa_1} + \beta^2\overline{\kappa_0}}{1 - \beta^2}\right). \tag{41}$$

We may now express c_G^2 in terms of GEODE intrinsic properties. If the GEODE crust rotates rigidly, then functions of $\beta(\eta)$ have no position dependence and commute through spatial averages. Substituting Equations (37) and (41) into Equation (36) gives

$$c_G^2 = \frac{1}{3}\left[\frac{2\langle\overline{\kappa_1}\rangle_{\mathcal{B}} + \gamma^2(\langle\overline{\kappa_1}\rangle_{\mathcal{B}} + \beta^2\langle\overline{\kappa_0}\rangle_{\mathcal{B}}) - 3u}{\gamma^2(\langle\overline{\kappa_0}\rangle_{\mathcal{B}} + \beta^2\langle\overline{\kappa_1}\rangle_{\mathcal{B}}) + u}\right]. \tag{42}$$

It is instructive to consider the two limits

$$c_G^2 = \begin{cases} -1 + \chi + \ldots & \beta \to 0 \\ 1/3 & \beta \to 1. \end{cases} \tag{43}$$

The nonspinning $\beta \to 0$ limit sets the squared sound speed of density perturbations equal to the background equation of state. As Hu (2004, Section 5.2) remarks, a DE model with this behavior will undergo accelerated clumping. This is consistent with expectations from Croker et al. (2020, Section 3). Pointlike GEODEs at small scales, without spin, aggregate more quickly due to blueshifting mass.

The rapidly spinning $\beta \to 1$ limit can be recognized as perceiving the crust as a nearly null flux, with equation of state 1/3. Like radiation overdensities, a GEODE population with very high spin will tend to disperse at first order.

5. Population III GEODE Dynamics at First Order

In the previous section, we established how the local structure and behavior of each individual GEODE defines the bulk fluid parameters χ and c_G^2. In this section, we construct the scalar mode equations appropriate[8] for this model. They will be

[8] The vector and tensor portions of the anisotropic stress can introduce vorticity and perturbations to the gravitational radiation field, respectively. Supposing vector anisotropic stresses come from the rotational motion of individual GEODEs, for all modes of interest with respect to large-scale structure, we expect these contributions to cancel. The possible role of tensor anisotropic stress from GEODEs is less clear, but it would only influence the gravitational radiation field, which does not affect large-scale structure.

characterized by three perturbation variables: density contrast

$$\delta_G := \frac{(\delta\rho_G)}{\rho_G}, \tag{44}$$

peculiar velocity v_G, and anisotropic stress Π_G. We use the density contrast instead of the density perturbation because it results in simpler equations and is more readily interpreted.

For simplicity, GEODEs interact with CDM and baryons only through the gravitational potentials Φ and Ψ. CDM will be tracked by two perturbation variables: density contrast $\delta_{\rm cdm}$ and peculiar velocity $v_{\rm cdm}$. Baryons will be tracked by two perturbation variables: density contrast δ_b and peculiar velocity v_b. With the exception of v_G, the evolution equations are standard and given in Appendix C. Initial conditions follow from continuity of the energy density and are given in Appendix D. In this section, the combination k/H occurs frequently. In our choice of units, this introduces dimensionful factors of

$$k_{\rm fac} := c/10^3 H_0. \tag{45}$$

5.1. GEODE Peculiar Velocity Field

The dynamics for the velocity field of any decoupled constituent are given in an arbitrary gauge by Hu (2004, Equation (19)),

$$\left[\frac{d}{d\eta} + 4\frac{\dot a}{a}\right](\rho_G + p_G)\frac{v_G - B}{k} = \delta p_G - \frac{2}{3}p_G\Pi_G + (\rho_G + p_G)\Psi. \tag{46}$$

Here B is the vector shift, which is defined to be 0 in Newtonian gauge, and we have set Hu's RW spatial curvature $K = 0$. Substituting the background equation of state from Equation (16) gives

$$\left[\frac{d}{d\eta} + 4\frac{\dot a}{a}\right]\chi\rho_G\frac{v_G - B}{k} = \delta p_G + \frac{2}{3}(1-\chi)\rho_G\Pi_G + \chi\rho_G\Psi. \tag{47}$$

A dynamical model for the peculiar velocity field requires the derivative term $\dot v_G$, so we divide by χ:

$$\left[\frac{d}{d\eta} + 4\frac{\dot a}{a}\right]\rho_G\frac{v_G - B}{k} = \chi^{-1}\delta p_G + \frac{2}{3}(\chi^{-1} - 1)\rho_G\Pi_G + \rho_G\Psi. \tag{48}$$

To model a population of individual DE point objects, however, we need to take $\chi \to 0$. Evidently, the dynamics cannot be perturbatively consistent in the $\chi \to 0$ limit unless

$$\delta p_G = -\frac{2}{3}\rho_G\Pi_G. \tag{49}$$

An algebraic relation between δp_G and Π_G is unsurprising, given Equation (27) and that $k \ll 1/R$. It is remarkable, however, that Equation (49) contains no explicit $\boldsymbol{k}$ dependence. The proportionality holds at all modes, not just modes below $\sim 1/R$. In other words, viable GEODE interiors must have nonvanishing anisotropic stress. This result is consistent with the conclusions of Cattoen et al. (2005), who found that a wide class of GEODEs must feature anisotropic stress. For $k \ll 1/R$, the GEODE anisotropic stress perturbation is determined by combining Equation (49) with Hu (2004, Equation (107)),

$$\Pi_G = -\frac{3}{2}\left[c_G^2\delta_G + 3\chi Ha\frac{v_G - B}{kk_{\rm fac}}(c_G^2 + 1 - \chi)\right]. \tag{50}$$

We are now in position to define the dynamics of the GEODE peculiar velocity field. Substitution of Equation (49) back into Equation (46) gives

$$\frac{\chi\rho_G}{k}\left[\dot v_G = \dot B + (3\chi - 4)(v_G - B)\frac{\dot a}{a} + k\Psi - \frac{2}{3}k\Pi_G\right]. \tag{51}$$

All quantities outside the square braces are nonzero, and we divide them off:

$$\dot v_G = \dot B + (3\chi - 4)(v_G - B)\frac{\dot a}{a} + k\Psi - \frac{2}{3}k\Pi_G. \tag{52}$$

This equation is true for an arbitrary gauge, so the dynamics of the Population III GEODE velocity field are well defined for arbitrarily small χ, provided that Equation (49) is satisfied. Fixing to Newtonian gauge, expressing derivatives in terms of the scale factor, scaling units, and rearranging give

$$\frac{dv_G}{da} = (3\chi - 4)\frac{v_G}{a} + \frac{kk_{\rm fac}}{Ha^2}\left(\Psi - \frac{2}{3}\Pi_G\right). \tag{53}$$

Note that GEODEs with $\chi \to 0$ have the largest possible "Hubble drag" consistent with the DEC.

5.2. GEODE Continuum Fluid Parameter Values

The model we have constructed has three constant parameters: the redshift of burst formation z_G, the deviation from perfect de Sitter interior $\chi > 0$, and the nonadiabatic sound speed c_G^2. The time of burst formation z_G affects the fraction of baryons Ξ required to produce the observed Ω_Λ. Planck determines a baryon density parameter at recombination:

$$\Omega_b h^2 = (2.2236 \pm 0.015) \times 10^{-2} \quad (68\%\ \text{confidence}). \tag{54}$$

GEODEs, however, form at much later times. Independent late-time measurements of Ω_b by Macquart et al. (2020) with fast radio bursts are consistent with the measured value at recombination, with 40% uncertainties.

We assume that the epoch of Population III star formation is $8 \leqslant z \leqslant 20$. In our cosmology, this occurs over $\sim$0.5 Gyr. Inoue et al. (2014, Figure 2) use the extragalactic background light (EBL) to place constraints on the Population III star formation rate (SFR). Based on this figure, an averaged SFR density for $z \leqslant 20$ is $\sim 5 \times 10^{-2} M_\odot\ {\rm yr}^{-1}\,{\rm Mpc}^{-3}$. Combining these estimates gives the following density in Population III stars,

$$\Omega_{\rm III} \sim 2 \times 10^{-4}, \tag{55}$$

expressed in units of the critical density today. No Population III star has been observed, so we regard the entirety of this fraction as collapsing and accreting onto GEODEs. Because the total baryon fraction is $\Omega_b \sim 0.05$, this means

$$\Xi \sim 4 \times 10^{-3}. \tag{56}$$

We combine this collapse fraction with the measured χ from Aghanim et al. (2018, Equation (51)),

$$\chi \leqslant 0.05 \qquad (95\% \text{ confidence}), \tag{57}$$

and use Equation (18) to estimate an approximate burst time,

$$z_G \sim \begin{cases} 15 & \chi \to 0.05 \\ 14 & \chi \to 0. \end{cases} \tag{58}$$

As expected, this value lies in the middle of our assumed Population III formation range.

We have ignored the details of accretion and dynamic spin-up in our simplified treatment. The approximate burst formation time given in Equation (58) is consistent with EBL constraints and regenerates the correct Ω_Λ. It need not be appropriate for inferring GEODE distribution in space. This is because GEODEs need not initially form with high spin and so may initially clump. There may be a delay between when GEODEs form and when GEODEs reach sufficient spin to dynamically repel. For dynamical studies, we will consider burst formation times over the entire Population III range,

$$8 \leqslant z_G \leqslant 20. \tag{59}$$

In order that the GEODE population resist collapse, $c_G^2 > 0$. From Equation (42), this requirement becomes

$$2\langle\overline{\kappa_1}\rangle_{\mathcal{B}} + \gamma^2(\langle\overline{\kappa_1}\rangle_{\mathcal{B}} + \beta^2\langle\overline{\kappa_0}\rangle_{\mathcal{B}}) > 3u. \tag{60}$$

Essentially, the boosted pressure within the crust must exceed the energy density of the de Sitter region by a factor of 3. We can develop a lower bound by assuming a dusty crust $\langle\overline{\kappa_1}\rangle := 0$,

$$\gamma^2\beta^2\chi > 3. \tag{61}$$

Evaluation with Equation (57) gives

$$\gamma \gtrsim 8. \tag{62}$$

In this regime, we may determine a constraint between c_G^2, χ, and γ:

$$c_G^2 \simeq \frac{1}{3} - \frac{4}{3\gamma^2\chi}. \tag{63}$$

A discussion of plausible γ and its relation to the Kerr solution can be found in Section 7.2. We will consider the following range of nonadiabatic squared sound speeds,

$$0 < c_G^2 < \frac{1}{3}. \tag{64}$$

6. Results

In the previous section, we established the appropriate dynamical equations, initial conditions, and parameter values for a late-time burst formation of Population III GEODEs from baryons. In this section, we present results from numerical integration of these equations: GEODE power spectra and GEODE-CDM cross-correlations.

6.1. Methods

We solved the initial value problem presented in Section 5, Appendices C, and D with the `odeint` package in Python 3.5. Initial conditions were determined using the CLASS Einstein–Boltzmann code (Blas et al. 2011). We verified the correct configuration of CLASS, and our analysis tool chain, by regenerating Planck's reported σ_8 to $<0.5\sigma$ from directly output Fourier mode amplitudes. We verified our Einstein code in two ways under ΛCDM assumptions. We regenerated an indistinguishable σ_8 by integrating from z_G with initial conditions generated by CLASS. We also regenerated σ_8 to $\sim$5% by integrating from primordial times, regarding baryons as CDM. In a Population III GEODE scenario, $\Omega_\Lambda = 0$ until the formation of GEODEs at z_G. Despite this, Ω_Λ set to the typical value at primordial times within the CLASS code can have only a negligible effect on all initial conditions used in this study.

6.2. GEODE Power Spectra

We consider two burst formation scenarios bracketing our assumed epoch of Population III star formation: $z_G = 20$ and $z_G = 8$. Figure 1 displays an early-burst formation at $z_G = 20$ for parameter values at log spacing. Initially, GEODEs start with spectra identical to baryons. For all parameter values, these spectra damp substantially during evolution. GEODE linear power for $z < 2$ is always suppressed by at least 10^5, relative to the peak linear CDM power $\sim 10^3$. Upon approach to the present day, depending on parameter space, GEODE power can become further suppressed by 10^3. In other words, early-burst GEODEs with $\gamma \gtrsim 8$ tend toward uniformity. They achieve near uniformity before the epoch of galaxy formation, and density contrast continues to damp during galaxy evolution.

Figure 2 displays a late-burst formation at $z_G = 8$ for parameter values at log spacing. We regard this scenario as a dynamical proxy to an earlier burst formation but with a spin-up delay. Initially, GEODEs start with spectra identical to baryons. Again, for all parameter values, the spectra damp substantially during evolution. GEODE linear power for $z < 2$ is always suppressed by at least 10^3, relative to peak linear CDM power $\sim 10^3$. Due to a later burst, oscillations about uniformity can persist through the epoch of galaxy formation until the present day. In other words, late-burst GEODEs with $\gamma \gtrsim 8$ also tend toward uniformity but can exhibit residual structure.

6.3. Late-burst Scenarios and Void-scale Anticorrelation

The first-order analysis we have performed cannot make strong statements about the distribution of Population III GEODEs above the nonlinearity scale $k_{\rm nl}$. For a late-burst scenario, possible structure can remain in the GEODE distribution. It is then of interest to ask under what circumstances do GEODEs become anticorrelated at the smallest scales accessible to linear theory. Consider anticorrelation achieved around the epoch of galaxy formation that persists until the present day. In such scenarios, it becomes even less likely that the nonlinear evolution of the GEODE density contrast would build significant overdensities on scales $\gtrsim k_{\rm nl}$.

To investigate this question, we compute the GEODE-CDM cross-correlation coefficient:

$$\xi(z) := \frac{\sum_k \delta_G(z,k)\delta_{\rm CDM}(z,k)}{\sqrt{\left(\sum_k \delta_G(z,k)^2\right)\left(\sum_k \delta_{\rm CDM}(z,k)^2\right)}}. \tag{65}$$

We restrict our attention to the high end of the linear theory $0.01 \leqslant k \leqslant k_{\rm nl}$. In Figure 3, we display smoothed values of

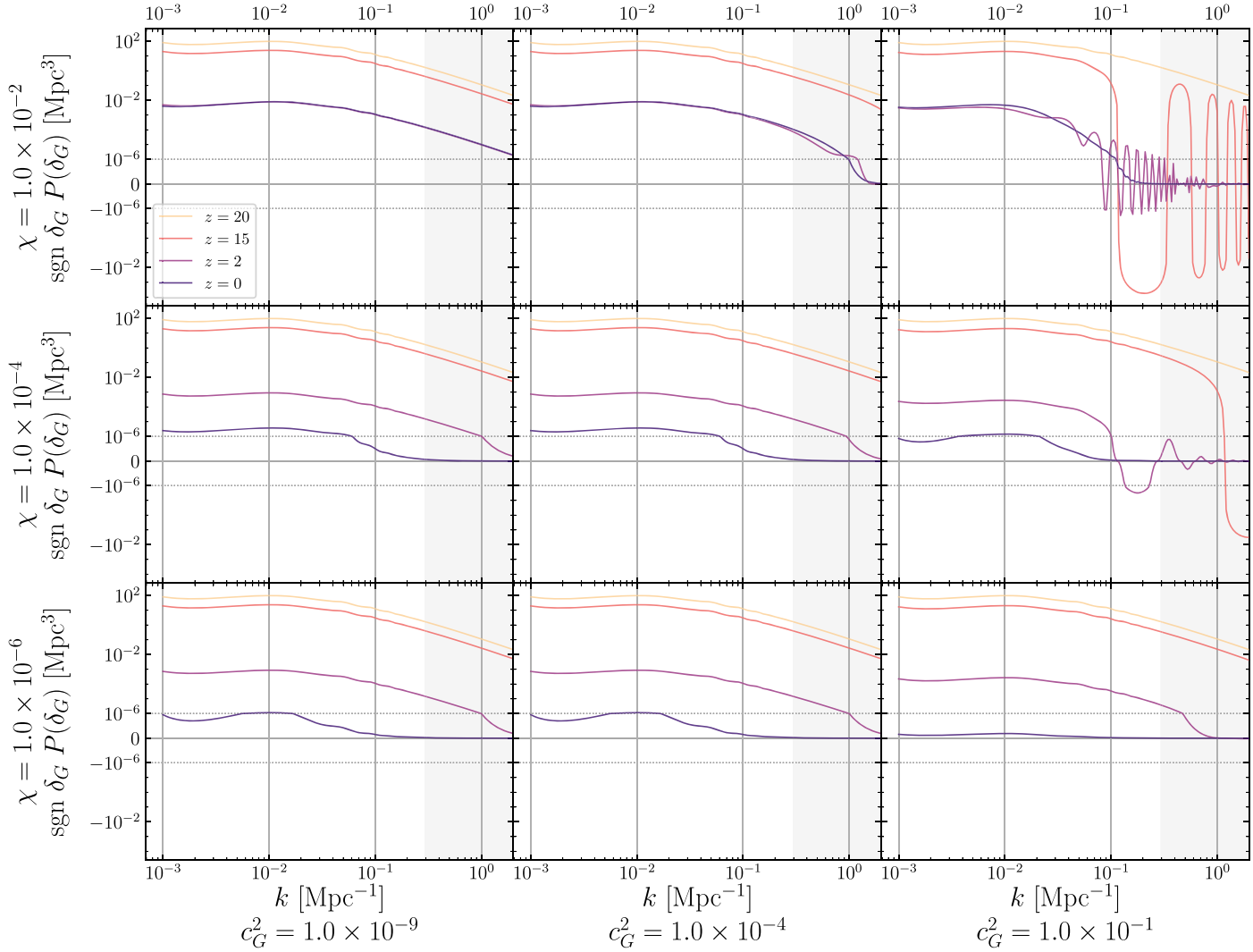

Figure 1. GEODE power spectra (autocorrelation) $P_G(k)$ and their time evolution for nine distinct burst formations at $z_G = 20$. Along the grid, nonadiabatic (i.e., perturbation) sound-speed squared c_G^2 increases to the right and deviation from a perfect de Sitter equation of state χ increases vertically. On each graph, vertical axes are displayed in a symmetric log scale, with a transition to linear axes at $\pm 10^{-6}$ (horizontal dotted). The nonlinearity regime, beginning at $k_{\rm nl} \sim 30$ Mpc, is shaded in gray. The temporal evolution of the spectra is shown in color (intensity). Initial values ($z = 20$) are perfectly correlated with the baryon density contrast δ_b and show inherited baryon acoustic oscillations (BAO). Except at high χ and low c_G^2, power in GEODE density contrast damps $\times 10^4 - \times 10^8$ toward zero. Present-day ($z = 0$) power at scales $\leqslant$100 Mpc is often essentially zero, implying uniform distribution at the scale of clusters. Acoustic oscillations in the GEODE population are visible at high c_G^2.

$\xi(0)$ determined from 400 uniform samples of parameter space for a burst formation at $z_G = 8$. Much of the parameter space produces GEODE populations that are weakly correlated or anticorrelated with CDM at the present day. Overlaid on this figure is also the requisite spin boost γ required to achieve the combination of χ and c_G^2. In Figure 4, we magnify the anticorrelated region of Figure 3. Overplotted contours represent regions of parameter space where the GEODE density contrast has been anticorrelated with CDM on average since $z < 2$. Evidently, regions of parameter space exist where GEODEs have been separate from CDM for $\sim$10 Gyr and remain so today.

7. Discussion

In the previous section, we presented results from the numerical solution of Einstein's equations at first order with a GEODE population at late times. In this section, we interpret these results physically. We then relate the spin of an individual GEODE to the spin of a Kerr BH. This allows us to place our assumptions and results in the context of existing observations.

7.1. Resolution of the MACHO Problem

All dynamics can be understood as damped oscillations about a uniformly distributed equilibrium. From Equation (27), the overpressure is c_G^2 times the density contrast. An appreciable and positive c_G^2 will cause Population III GEODEs to disperse from their progenitor baryonic overdensities. If they become underdense, gravitational attraction with CDM brings them back together. A large c_G^2 means greater pressures, and so larger amplitude oscillation and longer time to damp. Inspection of Equation (C4) reveals the effect of χ. A large χ implies less Hubble friction and greater sensitivity to the gravitational environment, and so more prone to oscillation. A large z_G implies earlier relaxation to low GEODE power. At small z_G,

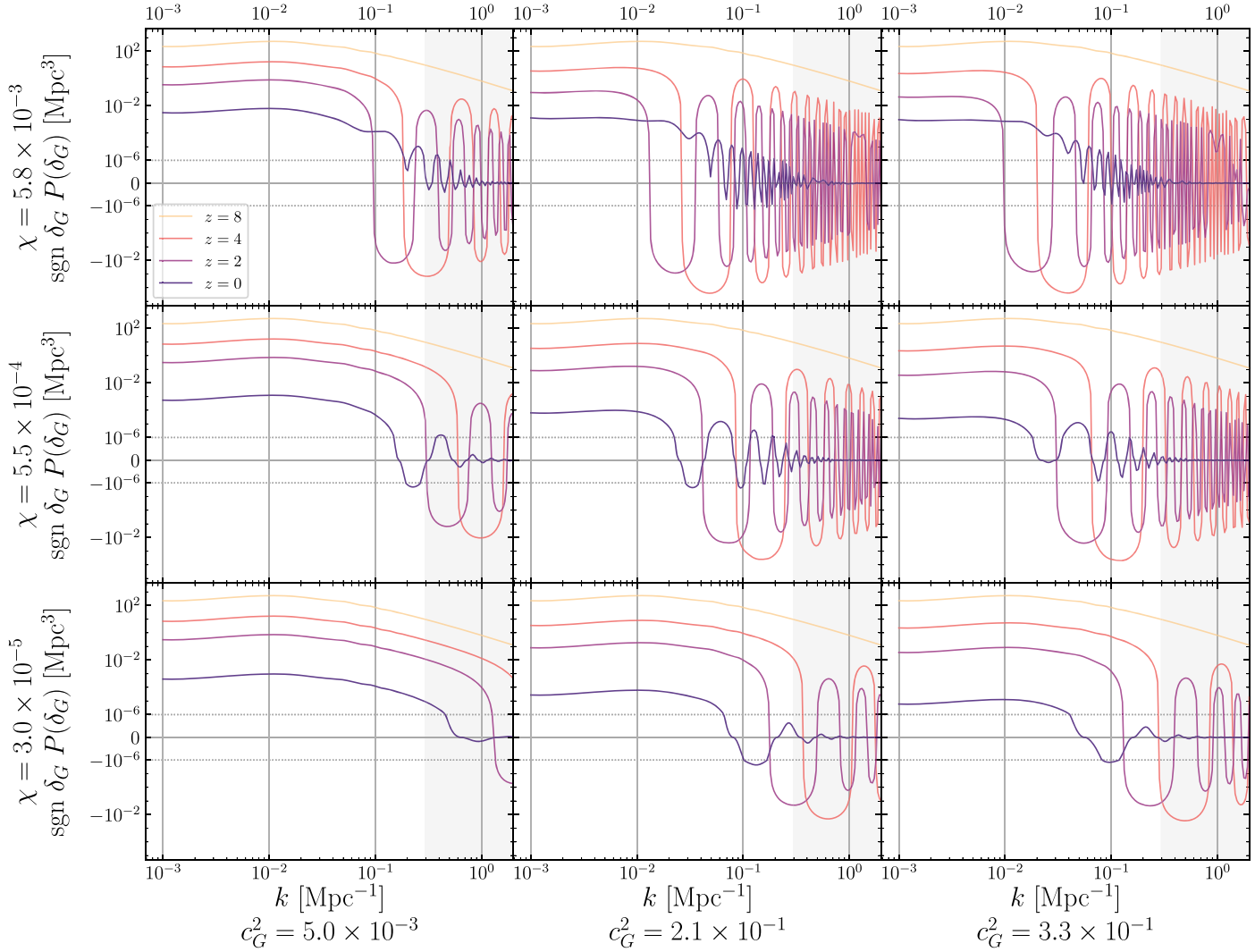

Figure 2. GEODE power spectra (autocorrelation) $P_G(k)$ and their time evolution for nine distinct burst formations at $z_G = 8$. Along the grid, nonadiabatic (i.e., perturbation) sound-speed squared c_G^2 increases to the right and deviation from a perfect de Sitter equation of state χ increases vertically. On each graph, vertical axes are displayed in a symmetric log scale, with a transition to linear axes at $\pm 10^{-6}$ (horizontal dotted). The nonlinearity regime, beginning at $k_{\rm nl} \sim 30$ Mpc, is shaded in gray. The temporal evolution of the spectra is shown in color (intensity). Initial values ($z = 8$) are perfectly correlated with the baryon density contrast δ_b and show inherited BAO. Over all parameter space displayed, power in GEODE density contrast damps $\times 10^4$ toward zero. Present-day ($z = 0$) power at scales $\leqslant$100 Mpc can exhibit oscillations, leading to anticorrelations.

matter overdensities have had more time to grow, so GEODE contrast will be more prone to oscillation.

MACHO constraints in the IMBH range are consistent with a density of disruptors $10^3 \rho_{\rm cr}$. We have shown that high-spin Population III GEODEs disperse and tend toward a uniform distribution with density Ω_Λ. In other words, Population III GEODEs are consistent with MACHO constraints over large ranges of parameter space.

7.2. Magnitude of GEODE γ, Relation to Kerr Spin

In Section 4, we found that GEODE peculiar flow has two regimes, depending on spin. For $\gamma \lesssim 8$, GEODEs undergo accelerated clustering. For $\gamma \gtrsim 8$, GEODEs effectively repel each other. To place this value for γ in context, contemporary terrestrial accelerators, such as the Large Hadron Collider (LHC; e.g., Evans & Bryant 2008), readily achieve proton beams with $\gamma > 10^3$. The radius of the LHC proton ring is $\sim$4.3 km, which is roughly the Schwarzschild radius of a 1 $M_\odot$ BH. Astrophysically, however, Hessels et al. (2006) report the fastest spinning pulsar has surface $\gamma = 1.03$.

Because GEODEs mimic BHs, it is of interest to relate γ to the Kerr dimensionless spin parameter a_*. A reasonable definition of tangential velocity for a Kerr hole is somewhat arcane. Smarr (1973, Equation (20)) gives a definition that may be expressed in terms of the Kerr dimensionless spin via Smarr (1973, Equations (11)). Converting to contemporary[9] notation, this relation becomes

$$\beta = \frac{\sqrt{1 - \sqrt{1 - a_*^2}}}{\sqrt{1 + \sqrt{1 - a_*^2}}} \qquad \gamma = \frac{1}{\sqrt{2}} \sqrt{1 + \frac{1}{\sqrt{1 - a_*^2}}}. \quad (66)$$

[9] Smarr (1973) uses a to mean the Kerr angular momentum per unit mass. The LIGO Scientific Collaboration et al. (2019) uses a to mean angular momentum per unit mass, in units of the Kerr (reducible) mass. To avoid collision of notation with the scale factor $a(\eta)$, we use a_* for the Kerr dimensionless spin.

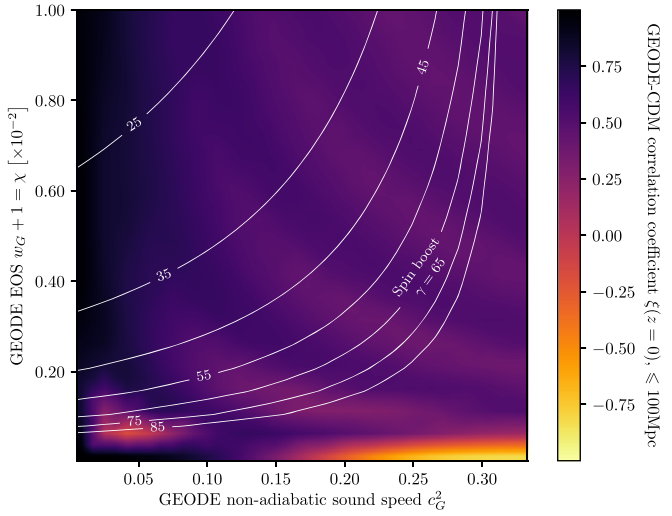

Figure 3. Correlation coefficient $\xi(z)$ (i.e., normalized Fourier-space dot product) of δ_G and $\delta_{\rm cdm}$. Heat map shows the present-day value $\xi(0)$ for scales greater than the nonlinearity scale $2\pi/k_{\rm nl} \sim 30$ Mpc and less than 100 Mpc. Unity indicates perfect correlation in space, while a negative one indicates perfect anticorrelation in space. Dependence is given in terms of the GEODE deviation from a perfect de Sitter equation of state χ and the nonadiabatic sound speed c_G^2. The GEODE spin Lorentz boost $\gamma(\chi, c_G^2)$ is overlaid as contours.

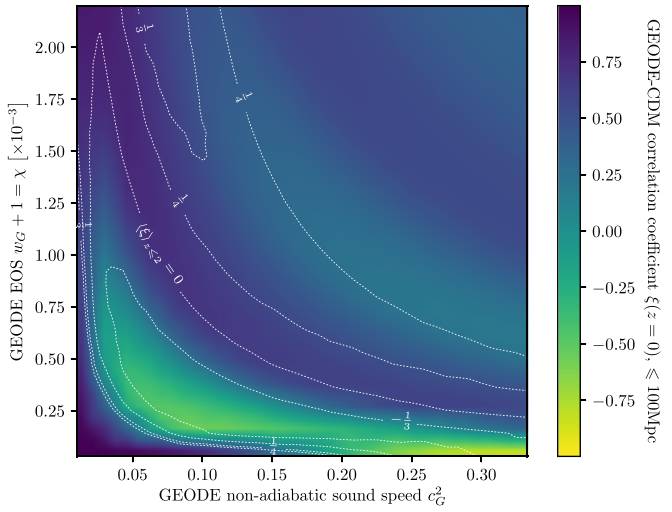

Figure 4. Detail of correlation coefficient $\xi(z)$ (i.e., normalized Fourier-space dot product) of δ_G and $\delta_{\rm cdm}$. The vertical axis is magnified by $\sim 5\times$, relative to Figure 3. The heat map has the same interpretation as Figure 3, though colors have been adjusted to distinguish the contours. The time-averaged correlation coefficient $\langle\xi\rangle$ for redshift $z \leqslant 2$ is overlaid as contours. Yellow (light) regions within the $-1/3$ contour have been anticorrelated for the past 10 Gyr and remain so today.

In order to achieve $\gamma \gtrsim 8$, we require a Kerr dimensionless spin

$$a_* > 0.99997. \tag{67}$$

The largest Kerr spin parameter measured by the LIGO Scientific Collaboration et al. (2019, Table III) is GW 170729, with $0.68 < a_* < 0.88$, which becomes $\gamma < 2.2$. Walton et al. (2016) report $0.93 \lesssim a_* \lesssim 0.96$ for the accreting X-ray binary BH Cygnus X-1, which becomes $\gamma \lesssim 3.2$. If these objects are also GEODEs, these data suggest that GEODEs do not initially have sufficient spin to enter the repulsive regime.

7.3. Time Dependence of GEODE γ

Repulsive behavior is required for GEODEs to be a viable late-time pointlike DE candidate. While this behavior is also superficially required for stability of the dynamical equations, β may be time dependent within the model we have considered. Assume a conservative $\gamma(z_G) \sim 2$, based on spin parameters reported by the LIGO Scientific Collaboration et al. (2019). In this regime, GEODE peculiar flow will undergo accelerated collapse.

Population III GEODEs form at an epoch with much higher density and from much larger progenitor stars. Given angular-momentum-conserving accretion due to GEODE blueshift and frequent mergers while in the accelerated collapse regime, Population III GEODEs with high spin are plausible. In fact, Bardeen (1970, Equation (4)) computes that $a_* \to 1$ as quickly as

$$m \to m_i \left\{ 1 + 3 \left[\sqrt{\sin^{-1}\left(\frac{2}{3}\right)} - \sin^{-1}\left(\frac{1}{3}\right) \right] \right\}, \tag{68}$$

where m_i is the Kerr mass at $a_* = 0$. In ideal settings, a 4 $M_\odot$ remnant with $a_* = 0$ will achieve $a_* = 1$ at $\sim 10 M_\odot$, if reached via accretion.

It must be emphasized that the Kerr solution is asymptotically flat and has a mass parameter that does not blueshift. Following the discussion in Croker & Weiner (2019, Section 3.1), Equation (68) can only be usefully applied in scenarios where accretion occurs much more rapidly than cosmological blueshift. The above factor in mass gain occurs from blueshift alone at

$$z_f \simeq \left(\frac{2}{3}\right)^{1/3} z_G. \tag{69}$$

For $z_G = 15$, blueshift has contributed the same mass required from accretion by $z_f = 13$, or 60 Myr later. This is equivalent to a constant accretion rate of $\sim 2.5 \times 10^{-7} M_\odot\ {\rm yr}^{-1}$. Accretion must be significantly larger than this, e.g., $\gtrsim 10^{-5} M_\odot\ {\rm yr}^{-1}$, to apply Equation (68). This would imply GEODE $\gamma \gg 8$ in as little as ~ 1 Myr. In this regime, the burst formation approximation we have studied is justified.

Under slower accretion rates, the appropriate spin-up time is unclear. This justifies studying the dynamics of a $z_G = 8$ burst scenario, with the implicit understanding that the baryon budget is adjusted with respect to an earlier formation $z_G \gtrsim 15$. The detailed study of the Population III GEODE scenario with time-dependent $\beta(\eta)$ is the subject of a future paper.

8. Conclusion

GEODEs are stellar collapse remnants with DE interiors. Cosmologically, they dilute in number density proportionally to the volume of the universe but blueshift in mass by a similar factor. An ensemble of GEODEs formed between $8 \lesssim z \lesssim 20$ will blueshift into an ensemble of $\sim 10^3$–$10^5\ M_\odot$ ultracompact objects today. Their resulting approximately constant physical density mimics Ω_Λ.

We have argued that such Population III stellar collapse GEODEs viably explain late-time accelerated expansion. To achieve this, we constructed a well-defined source to Einstein's equations perturbed about an isotropic and homogeneous background. The appropriate continuum fluid approximation to the unapproximated stress tensor contributions to Einstein's equations involves the truncated Fourier transform. This cutoff,

the nonlinearity scale $k_{\rm nl}$, is observable and is the first-order analog of the zero-order homogeneity scale. The resulting continuum fluid sources become smoothed: power on small scales is redistributed into the low Fourier modes described by linear theory. Consequently, the internal dynamics of ultra-compact objects can govern their peculiar flow at first order.

We presented the simplest schematic model of a GEODE. We used this model to compute the continuum fluid source's adiabatic and nonadiabatic sound speeds. The nonadiabatic sound speed has two dynamical regimes that depend on the spin of individual GEODEs. In the low-spin limit, GEODEs undergo accelerated clumping consistent with established literature. In the high-spin limit, GEODEs are expected to repel each other at large scales.

To investigate these dynamics, we solved Einstein's equations numerically with CDM, baryons, and a GEODE source. The presence of high-spin GEODEs does not significantly alter the power spectrum of CDM. The GEODE power spectra show that the GEODE density contrast damps to zero over most of the parameter space. Further, regions of parameter space exist where GEODE density contrast is uncorrelated or even anticorrelated with CDM. This establishes that Population III GEODEs do not preferentially aggregate with CDM over large regions of parameter space. In other words, MACHO constraints on intermediate-mass objects cannot be applied to exclude a Population III GEODE scenario.

We thank an anonymous referee for a penetrating question about the observational implications of the existence of GEODEs. In addition, we warmly acknowledge: J. Weiner (Hawai'i) for the proof in Appendix A and thorough technical review strengthening the work; N. Warrington (INT) for assistance during numerical implementation; and I. Szapudi (IfA) for feedback and stimulating discussions.

Software: CLASS[10] (Blas et al. 2011), `scipy`[11] (Oliphant 2007), Maxima[12] (Maxima 2019), matplotlib[13] (Hunter 2007).

Appendix A
Nonvanishing Sum of Phases

For N unequal points $\boldsymbol{x}_j \in \mathbb{R}^3$ fixed, consider

$$S(\boldsymbol{k}) \coloneqq \sum_{j=1}^{N} e^{i\boldsymbol{k}\cdot\boldsymbol{x}_j} \coloneqq \sum_{j=1}^{N} z_j(\boldsymbol{k}). \tag{A1}$$

Note that $S(\boldsymbol{k})$ is defined on $\mathbb{R}^3$ and can be regarded as a mapping to $\mathbb{R}^2$ via the standard isomorphism between $\mathbb{C}$:

$$S(\boldsymbol{k}) = \begin{pmatrix} \sum_{j=1}^{N} \cos\left[\boldsymbol{k}\cdot\boldsymbol{x}_j\right] \\ \sum_{j=1}^{N} \sin\left[\boldsymbol{k}\cdot\boldsymbol{x}_j\right] \end{pmatrix}. \tag{A2}$$

Thus, $S(\boldsymbol{k})$ is a finite sum of functions real analytic on $\mathbb{R}^3$, so it is also real analytic on $\mathbb{R}^3$. Even though Section 4 necessarily considers $S(\boldsymbol{k})$ on restricted domains $|\boldsymbol{k}|R \ll 1$, we will prove properties of $S(\boldsymbol{k})$ on all of $\mathbb{R}^3$. Our results will then hold on arbitrary open neighborhoods, such as all those within such restricted domains. Let

$$F(S) \coloneqq \{\boldsymbol{k}\colon S(\boldsymbol{k}) = 0\} \tag{A3}$$

be the zero set of S. To establish that this sum is nonvanishing a.e., we use an elementary result.

Theorem 1. *Let $S(\boldsymbol{k})\colon \mathbb{R}^n \to \mathbb{R}^m$ be real analytic. Then either $S(\boldsymbol{k}) = 0$ identically or $\mathrm{F(S)}$ has zero measure.*

A proof is given explicitly by Mityagin (2020). We will prove that $S(\boldsymbol{k})$ does not identically vanish.

Proof. Suppose for contradiction that $S(\boldsymbol{k}) = 0$ identically. Then, it follows that $S(m\boldsymbol{k}) = 0$ for all $m \in \mathbb{N}$, so

$$\sum_{j=1}^{N} [z_j(\boldsymbol{k})]^m = 0. \tag{A4}$$

Every order $L \geqslant N$ polynomial $p(z)$ over $\mathbb{C}$, without a constant term, may be written as

$$p(z) = \sum_{\ell=1}^{L} a_\ell z^\ell \qquad a_\ell \in \mathbb{C}. \tag{A5}$$

By supposition, it follows that the sum of $p(z_j)$ satisfies

$$\sum_{j=1}^{N} p(z_j) = \sum_{j=1}^{N}\sum_{\ell=1}^{L} a_\ell [z_j(\boldsymbol{k})]^\ell \tag{A6}$$

$$= \sum_{\ell=1}^{L} a_\ell \sum_{j=1}^{N} [z_j(\boldsymbol{k})]^\ell \tag{A7}$$

$$= 0. \tag{A8}$$

As no two GEODEs are located at the same place, $i \neq j \Rightarrow \boldsymbol{x}_j \neq \boldsymbol{x}_j$. Many z_j, however, could be equal in highly pathological (e.g., periodic) arrangements. Because each $z_j \neq 0$ by definition, there must be at least two nonequal z_j so that $S(\boldsymbol{k})$ can cancel to zero. Let w_j be the $1 < N_M \leqslant N$ distinct z_j and M_j their multiplicities. Define a particular order N polynomial $p(z)$ via its unique factorization over $\mathbb{C}$,

$$p(w) \coloneqq w \prod_{j>1}^{N_M} (w - w_j)^{M_j}. \tag{A9}$$

From this definition, it follows immediately that

$$\sum_{j>1}^{N_M} M_j p(w_j) = 0. \tag{A10}$$

But we know from Equation (A8)

$$M_1 p(w_1) + \sum_{j>1}^{N_M} M_j p(w_j) = 0, \tag{A11}$$

which implies that $p(w_1) = 0$. The contradiction is encountered: $p(w_1) \neq 0$ explicitly by Equation (A9). Thus, there exists an m such that $S(m\boldsymbol{k}) \neq 0$.

□

Appendix B
Transformation from an Eigenframe to an RW Frame

As discussed in Section 4, the typical formalism (e.g., Bardeen 1980) has no means to determine the necessary first-order sources

[10] https://lesgourg.github.io/class_public/class.html
[11] https://www.scipy.org
[12] http://maxima.sourceforge.net
[13] https://matplotlib.org/

from the unapproximated stress. We define our sources generically by use of eigenframe fields. In this appendix, we show how to relate the eigenframe fields to any RW frame fields.

B.1. Associated Vierbein Frame Fields

The eigenframe fields are definitive: they are physical, and so do not depend on arbitrary choices of "the user," such as the metric ansatz. A key virtue of eigenframe fields is that they are orthonormal. In eigenframe fields, the unapproximated metric has the canonical Minkowski representation

$$g_{\mu\nu} = \mathrm{diag}(-1, 1, 1, 1). \tag{B1}$$

Pick any point P. All subsequent discussion will apply to frames at this point, so we will stop explicitly saying "at P." In an eigenframe, the metric representation is canonical Minkowski. If we perform a Lorentz transformation, the metric representation does not change. In general, we are no longer in an eigenframe, because our frame is now spacetime rotated relative to the eigenframe. We are, however, still in an orthonormal frame (as evidenced by the canonical metric representation). In general, every orthonormal frame is related to every other orthonormal frame by some Lorentz transformation. We will leverage this fact to connect the eigenframe to the RW frame.

Our first goal is to construct an orthonormal frame from any RW frame. We will call this frame the "associated vierbein frame." The procedure is as follows:

1. Pick any RW frame for which the representation is defined (e.g., like Equation (5)).
2. The lowered metric representation gives the RW frame basis overlaps:

$$g_{\mu\nu} = \begin{bmatrix} \partial_0 \cdot \partial_0 & \cdots & \partial_0 \cdot \partial_3 \\ \vdots & \ddots & \vdots \\ \partial_3 \cdot \partial_0 & \cdots & \partial_3 \cdot \partial_3 \end{bmatrix}. \tag{B2}$$

   These inner products can be used in the Gram-Schmidt procedure to determine an orthonormal basis $\{v_\mu\}$, in terms of the RW frame coordinate basis $\{\partial_\mu\}$. This can always be done because the metric is semi-Riemannian and assumed to be well defined everywhere on $\mathcal{M}$.
3. Arrange the orthonormalized basis vectors (expressed with components from the RW frame representation) as rows in a table of numbers V^μ_σ.

The change of basis matrix V^μ_σ is sometimes called the vierbein. In our setting, V^μ_σ transforms from the RW frame $\{\partial_\mu\}$ into the associated vierbein frame $\{v_\mu\}$. The qualifier "associated" arises because the construction procedure takes as input some RW frame. Different RW frames will have different associated vierbein frames, in general.

B.2. Completing the Transformation

Now that we have an associated vierbein frame, we may complete the transformation from the eigenframe to the RW frame. Because the associated vierbein frame is orthonormal, it is always related to the eigenframe by a Lorentz transformation. Let Λ be a boost representing the four-velocity from the eigenframe to the associated vierbein frame. Let V represent the associated vierbein and A be its inverse. Then,

$$T_{\mu\nu} = A^\lambda_\mu \Lambda^\sigma_\lambda \overline{T_{\rho\sigma}} \Lambda^\rho_\tau A^\tau_\nu. \tag{B3}$$

It can be verified that this procedure regenerates Bardeen (1980, Equations (2.17)–(2.20)) under three assumptions: the boost velocity is defined to be order ϵ, the source is cleaved into a background and an order ϵ perturbation, and one computes with the vierbein frame associated with Equation (5).

Source term representations in the RW frame fields can now be determined without explicit prescription of coordinate bases for the strong sources. No other knowledge is required except that the coordinates of the RW frame field remain well defined on open sets containing the source. In this sense, our procedure is a relativistic generalization of the procedure outlined by Bardeen (1980, Section IIA).

B.3. GEODE Eigenframe to GEODE Flow Frame

We now have sufficient machinery to determine the transformation required in Section 4.4. To enter the associated vierbein frame from the eigenframe, two separate boosts must be performed. Because boosts are closed under composition, Equation (B3) continues to apply. The first boost introduces the tangential velocity due to spin at P. The second boost introduces the peculiar center -of-mass-motion.

There is never any Hubble flow contribution, because all RW frame fields are built from comoving coordinates. The second boost is required because the "flow gauge" is designed to remove energy flux T^0_k in RW frame fields that originally perceived it. Two separate boosts are required because vector four-velocity addition is incorrect in special relativity. The two successive boosts introduce a Thomas rotation and, in general, do not commute. This does not affect the isotropic pressure or energy density.

Finally, the inverse vierbein is applied to enter the flow frame. Clearly, this can only introduce order-ϵ adjustments. This procedure has been symbolically verified, in general, to produce T^0_k with only spin contributions, as expected. The diagonal components combine as indicated in Equations (37) and (41).

Appendix C
Typical First-order Equations

In this section, we present the first-order equations that follow rote from Hu (2004) and substitution of the model as defined in Section 5.

C.1. GEODE Density Contrast

The GEODE density contrast is defined as

$$\delta_G := \frac{\delta\rho_G}{\rho_G}, \tag{C1}$$

where $\delta\rho_G$ is the GEODE density perturbation. This quantity is -1 in true vacuum and 0 in regions where the local density is equal to the background. The continuity equation at first order for a decoupled component is given by Hu (2004, Section 3.3, Equation (33)):

$$\left(\frac{d}{d\eta} + 3\frac{\dot{a}}{a}\right)\delta\rho_G + 3\frac{\dot{a}}{a}\delta p_G = -(\rho_G + p_G)(kv_G + 3\dot{\Phi}). \tag{C2}$$

Substituting the GEODE background evolution from Equation (17), the anisotropic stress from Equation (49), and the definition of the density contrast gives

$$\frac{d\delta_G}{d\eta} + 3(1-\chi)\frac{\dot{a}}{a}\delta_G - 2\frac{\dot{a}}{a}\Pi_G = -\chi(kv_G + 3\dot{\Phi}) \quad \text{(C3)}$$

after evaluation of the derivative. Switching to scale factor and scaling gives the desired dynamical equation,

$$\frac{d\delta_G}{da} = 3(\chi-1)\frac{\delta_G}{a} + \frac{2\Pi_G}{a} - \chi\left(\frac{kk_{\rm fac}}{Ha^2}v_G + 3\frac{d\Phi}{da}\right). \quad \text{(C4)}$$

C.2. CDM and Baryons: Density Contrast and Peculiar Velocity Field

We adopt the standard CDM evolution equations and regard baryons at $z < 45$ as essentially dust. This means that baryons and CDM will have the same evolution equations; their dynamics will only differ by their initial conditions set at z_G. We will now use the subscript m for matter.

The velocity evolution equation for matter is equal to Equation (53), with the subscript G replaced with m, $\chi \to 1$, and $\Pi_m := 0$:

$$\frac{dv_m}{da} = -\frac{v_m}{a} + \frac{kk_{\rm fac}}{Ha^2}\Psi. \quad \text{(C5)}$$

Again, we will compute with the density contrast

$$\delta_m := \frac{\delta\rho_m}{\rho_m}. \quad \text{(C6)}$$

Substitution of this definition into the continuity Equation (C2) gives

$$\dot{\delta}_m = -kv_m - 3\dot{\Phi}. \quad \text{(C7)}$$

Switching to scale factor and rescaling units give the desired dynamical equation:

$$\frac{d\delta_m}{da} = -\frac{kk_{\rm fac}v_m}{Ha^2} - 3\frac{d\Phi}{da}. \quad \text{(C8)}$$

Note that this equation agrees with Equation (C4) when $\chi := 1$ and $\Pi_G := 0$. This completes the specification of the material bulk degrees of freedom describing the CDM and baryon-tracking fluids at late times.

C.3. The Einstein Equations

The Einstein equations are entirely determined via the action principle, the solution ansatz, and the choice of gauge. For ease of comparison with existing literature, we will express the dynamics in terms of the Newtonian scalar curvature Φ. Combine Hu (2004, Equations 17(a), (c)) and fix the gauge to Newtonian to find

$$k^2\Phi = 4\pi Ga^2\rho_{\rm cr}\sum_J \delta\rho_J + 3\frac{\dot{a}}{a}\left(\frac{\dot{a}}{a}\Psi - \dot{\Phi}\right), \quad \text{(C9)}$$

where we define the dimensionless sum of density perturbations as

$$\sum_J \delta\rho_J := \Omega_m a^{-3}\delta_m + \Omega_\Lambda a^{-3\chi}\delta_G. \quad \text{(C10)}$$

Hu (2004, Equation (17)) gives the algebraic relation between the gravitational potentials and the anisotropic stress perturbation:

$$k^2(\Psi+\Phi) = -8\pi Ga^2 p_G \Pi_G, \quad \text{(C11)}$$

where we have fixed to Newtonian gauge. Note that GEODEs are the only relevant source of anisotropic stress. Rearranging, substituting the background evolution, and scaling give

$$\Psi = \frac{3(1-\chi)a^{2-3\chi}\Omega_\Lambda\Pi_G}{k^2k_{\rm fac}^2} - \Phi. \quad \text{(C12)}$$

Rearranging, switching to scale factor, and scaling the remaining terms give the desired dynamical equation for the Newtonian scalar curvature:

$$\frac{d\Phi}{da} = -\frac{ak^2k_{\rm fac}^2\Phi}{3H^2a^4} + \frac{a^3\sum_J\delta\rho_J}{2H^2a^4} + \frac{\Psi}{a}. \quad \text{(C13)}$$

This completes the specification of the scalar gravitational degrees of freedom.

Appendix D
Initial Conditions

At first order in the perturbation, we have seven, first-order, differential equations for seven degrees of freedom: Φ, $v_{\rm cdm}$, $\delta_{\rm cdm}$, v_b, δ_b, v_G, and δ_G. Because a burst formation involves a Dirac delta function in time, initial conditions are determined in the limit of $a_G \pm \epsilon$ for $\epsilon \to 0$. We will omit writing the limit explicitly, instead writing a_G^- and a_G^+ for the left and right limits, respectively.

We define the GEODE bias b_G so that

$$\delta_G(a_G^+) := b_G\delta_b(a_G^-). \quad \text{(D1)}$$

If $b_G = 0$, then the initial GEODE density contrast is zero and so GEODEs are produced uniformly everywhere. If $b_G = 1$, then the initial GEODE density contrast identically tracks the baryon distribution. Because we assume stellar progenitors to Population III GEODEs, there is little physical motivation to consider $b_G \leqslant 0$. In principle, the bias could depend on k, but for simplicity we do not consider such possibilities in this work.

To determine the initial condition for the matter density contrast, we enforce that the overall energy density be continuous at a_G:

$$[\rho_b(1+\delta_b) + \rho_G(1+\delta_G)]|_{a_G^+} = [\rho_b(1+\delta_b)]|_{a_G^-}. \quad \text{(D2)}$$

Note that we have omitted the CDM contribution $\rho_{\rm cdm}(1+\delta_{\rm cdm})$ because we do not deplete CDM when forming GEODEs. This equation can be solved for the baryon density contrast immediately after the burst:

$$\delta_b(a_G^+) = \left(\frac{1-b_G\Xi}{1-\Xi}\right)\delta_b(a_G^-). \quad \text{(D3)}$$

The velocity field of the matter should not initially be changed by the formation of GEODEs, so

$$v_{\rm cdm}(a_G^+) := v_{\rm cdm}(a_G^-) \quad \text{(D4)}$$

$$v_b(a_G^+) := v_b(a_G^-). \quad \text{(D5)}$$

Similarly, any GEODEs formed should initially be flowing identically with the baryons whence they came,

$$v_G(a_G^+) := v_b(a_G^-). \quad \text{(D6)}$$

All other initial conditions are unaltered.

ORCID iDs

K. S. Croker https://orcid.org/0000-0002-6917-0214
J. Runburg https://orcid.org/0000-0001-9921-7100
D. Farrah https://orcid.org/0000-0003-1748-2010

References

Aghanim, N., Akrami, Y., Ashdown, M., et al. 2018, arXiv:1807.06209
Amendola, L., & Tsujikawa, S. 2010, Dark Energy: Theory and Observations (Cambridge: Cambridge Univ. Press)
Bardeen, J. M. 1970, Natur, 226, 64
Bardeen, J. M. 1980, PhRvD, 22, 1882
Binney, J., & Tremaine, S. 2008, Galactic Dynamics (HB) (Princeton, NJ: Princeton Univ. Press)
Blas, D., Lesgourgues, J., & Tram, T. 2011, JCAP, 2011, 034
Cattoen, C., Faber, T., & Visser, M. 2005, CQGra, 22, 4189
Croker, K. S., Nishimura, K., & Farrah, D. 2020, ApJ, 889, 115
Croker, K. S., & Weiner, J. L. 2019, ApJ, 882, 19
D'Eath, P. 1976, AnPhy, 98, 237
Dodelson, S. 2003, Modern Cosmology (New York: Academic)
Evans, L., & Bryant, P. 2008, JInst, 3, S08001
Gliner, E. B. 1966, JETP, 22, 378
Hessels, J. W., Ransom, S. M., Stairs, I. H., et al. 2006, Sci, 311, 1901
Hu, W. 2004, arXiv:astro-ph/0402060
Hunter, J. D. 2007, CSE, 9, 90
Inoue, Y., Tanaka, Y. T., Madejski, G. M., & Domínguez, A. 2014, ApJL, 781, L35
Landau, L. D., & Lifshitz, E. M. 1959, Fluid Mechanics (Oxford: Pergamon)
LIGO Scientific Collaboration, Virgo Collaboration et al. 2019, PhRvX, 9, 031040
Macquart, J.-P., Prochaska, J., McQuinn, M., et al. 2020, Natur, 581, 391
Maxima 2019, Maxima, a Computer Algebra System. Version 5.38.1, http://maxima.sourceforge.net/
Mityagin, B. S. 2020, Matematicheskie Zametki, 107, 473
Monroy-Rodríguez, M. A., & Allen, C. 2014, ApJ, 790, 159
Oliphant, T. E. 2007, CSE, 9, 10
Peebles, P. J. E. 1980, The Large-scale Structure of the Universe (Princeton, NJ: Princeton Univ. Press)
Perlmutter, S., Aldering, G., Goldhaber, G., et al. 1999, ApJ, 517, 565
Riess, A. G., Filippenko, A. V., Challis, P., et al. 1998, AJ, 116, 1009
Smarr, L. 1973, PhRvD, 7, 289
Walton, D., Tomsick, J., Madsen, K., et al. 2016, ApJ, 826, 87